Radiative and microphysical properties of Arctic stratus clouds from multiangle downwelling infrared radiances

Carsten Rathke,[1] Steven Neshyba,[2] Matthew D. Shupe,[3] Penny Rowe,[4] and Aaron Rivers[5]

[1]   The information content of multiangle downwelling infrared radiance spectra of stratus clouds is investigated. As an example, 76 sets of spectra were measured at angles of 0, 15, 30 and 45° from zenith, using an interferometer based at the Surface Heat Budget of the Arctic Ocean (SHEBA) drifting ice camp. Exploiting the angular variation of radiance in infrared microwindows, a "geometric" algorithm is used to determine cloud temperature and optical depth without auxiliary information. For comparison, a spectral method allows us to infer cloud microphysical properties for each angle; each multiangle set therefore constitutes a microphysical characterization of horizontal inhomogeneity of the cloudy scene. We show that cloud temperatures determined with both approaches agree with temperatures obtained from lidar/radiosonde data. The multiangle radiance observations can also be used to calculate the longwave flux reaching the surface. We find that up to 14 W m^{-2} of the overcast fluxes can be attributed to horizontal variations in cloud microphysical properties.   INDEX TERMS: 0320 Atmospheric Composition and Structure: Cloud physics and chemistry; 0360 Atmospheric Composition and Structure: Transmission and scattering of radiation; 3359 Meteorology and Atmospheric Dynamics: Radiative processes; 3360 Meteorology and Atmospheric Dynamics: Remote sensing; KEYWORDS: infrared emission, Arctic clouds, multiangle FTIR Spectroscopy, horizontal inhomogeneity, longwave flux, SHEBA

1.   Introduction

[2]   The Arctic climate is strongly influenced by an extensive and persistent pattern of cloud cover [Francis, 1997]. During transition seasons, the predominant form is a thin, mixed-phase boundary-layer cloud topped by an inversion layer [Pinto et al., 1997]. Theoretical studies show that these clouds modulate the column temperature by accelerating cooling of the atmosphere and slowing down cooling of the surface [Curry et al., 1996]. Models also show that Arctic ice thickness is highly sensitive to changes in downwelling radiation fluxes [Thorndike, 1992]. Because the clouds are thin, small changes in microphysical and bulk properties can have significant effects on long-wave radiation, which dominates the radiation energy budget between midautumn to midspring. Altogether, these considerations motivate the present study.

[3]   In the Arctic region, retrieval of properties of low clouds by remote sensing from aircraft or satellite is complicated by the difficulty in discriminating those clouds from the snow- and ice-covered surface in the visible, infrared and microwave spectral ranges [Curry et al., 1996; Francis, 1997]. Hence there is considerable interest in developing improved surface-based remote sensing techniques for probing Arctic stratus clouds and providing validation data for satellite retrievals and climate-model results.

[4]   Ground-based infrared spectrometry has been used in many settings to derive cloud properties [Smith et al., 1993; Rathke et al., 2000, and the references therein]. Commonly, clouds are observed at a single zenith-angle and the retrievals use the frequency dependence of the clouds' thermal emission in the 750–1250 cm^{-1} spectral region. We will call this technique the "spectral" method of analysis to distinguish it from the "geometric" method introduced below. Thermal emission is a function of cloud height, thickness, temperature, phase, water content, and particle size. Most spectral retrieval algorithms benefit greatly from radiosonde profiles and lidar data that can help characterize cloud height and temperature as well as the trace gas contribution to the downwelling radiance. However, special difficulties are encountered in remote geographic regions

[1]Institut für Weltraumwissenschaften, Freie Universität Berlin, Berlin, Germany.
[2]Chemistry Department, University of Puget Sound, Tacoma, Washington, USA..
[3]Science and Technology Corporation, NOAA/Environmental Technology Laboratory, Boulder, Colorado, USA.
[4]Department of Chemistry, University of Washington, Seattle, Washington, USA.
[5]Cooperative Institute for Research in Environmental Sciences, University of Colorado, Boulder, Colorado, USA.

such as the Arctic, where facilities for obtaining auxiliary information are sparse. *Lubin and Simpson* [1997] therefore reported retrievals of Arctic cloud properties using downwelling infrared radiances alone; but it is difficult to estimate the accuracy of such retrievals without corroborating information of some kind.

[5] In this context, we have reconsidered the opportunities offered by infrared observations at multiple angles. First, for remote sensing of plane-parallel clouds, multiangle observations offer the advantage of not requiring auxiliary data. *Taylor* [1974] initially proposed remotely sensing cloud optical depth, cloud temperature and surface temperature from three measurements at different zenith angles. We call this technique the "geometric" method. *Prata and Barton* [1993] developed from that idea an operational algorithm for the retrieval of cloud optical depth from dual-angle, dual-wavelengths thermal-IR measurements made by the Along Track Scanning Radiometer (ATSR) satellite instrument. As discussed by *Diner et al.* [1999], multiangle sensing in general provides better constraints, leading to more accurate retrievals of cloud properties.

[6] In practice, the problem is to obtain the necessary angular coverage with one instrument within a time scale over which the scene does not vary substantially, and to ensure that the plane-parallel assumption is valid. Some radiative models of Arctic stratus clouds have achieved considerable success in predicting the angular distribution of radiance by assuming that clouds have plane-parallel geometry. *Makshtas and Korsnes* [2001], for example, have reported that surface measurements of the angular and spectral redistribution of solar radiation are well reproduced using this assumption. In contrast, other measurements have suggested that horizontal inhomogeneity of a cloudy scene can cause substantial biases in surface [*Lubin and Simpson*, 1997] and top-of-atmosphere [*Fu et al.*, 2000] longwave fluxes. A second opportunity offered by multiangle measurements is the possibility of characterizing this inhomogeneity in terms of cloud microphysical properties, even in apparently plane-parallel overcast conditions.

[7] This paper demonstrates the potential improvements to infrared remote sensing of Arctic clouds when surface-based measurements are made at multiple angles. The structure of the paper is as follows. Section 2 provides details about a ship-based interferometer, the University of Puget Sound Fourier Transform Infrared Spectroradiometer (UPS-FTIR), with which cloud spectra were recorded at four zenith angles during March and April 1998 as part of the SHEBA experiment [*Uttal et al.*, 2002]. The measurements were conducted during conditions thought to represent homogeneous, plane-parallel stratus clouds. Section 3.1 introduces the geometric method for ground-based sensing and for retrievals of cloud temperature and optical depth, and tests developed for its use, such as the "straight-line criterion". Section 3.2 gives a description of the spectral method for the analysis of single-angle spectra. Section 4 provides the results obtained with the geometric and spectral methods, and their comparison with independent information derived from lidar and radiosonde data. The results are also used to quantify the horizontal variability of cloud properties over distances

of 0.1 to 5 km and their effect on downwelling longwave fluxes.

2. Instrumentation and Measurements

[8] The UPS-FTIR is a Bruker IFS-55 Fourier transform infrared spectrometer that measures the thermal radiance emitted by clouds and atmospheric gases in an absolutely calibrated, spectrally resolved way. Its architecture is similar to other remote sensing interferometers, such as the Atmospheric Emitted Radiance Interferometer (AERI) [*Smith et al.*, 1993], in that it is equipped with two temperature-controlled blackbodies for calibration, and external optics for transmitting downwelling radiance into the instrument. The instrument has a maximum resolution of 0.2 cm^{-1}; it was operated here at 1.1 cm^{-1}. The full angle field-of-view is about 2.5°. The detector is a Mercury-Cadmium-Telluride composite with sensitivity greater than 10% of maximum in the range 500–2500 cm^{-1}. The calibration blackbodies are constructed from an aluminum cylinder whose surface was milled into 1 mm deep groves, painted with a commercial flat black paint, and set in an insulated housing.

[9] During the SHEBA campaign, the UPS-FTIR was positioned on the deck of the Canadian icebreaker *Des Groseilliers*, which was frozen into the Arctic Ocean ice pack. From March to April 1998, the ship drifted from (75.5°N, 160°W) to (76°N, 166°W). The azimuthal direction in which the measurements were made depended on the actual heading of the ship. Spectra were obtained at zenith angles of θ = 0°, 15°, 30°, and 45°, during cloudy conditions which appeared plane-parallel to a ground observer. Such a sequence of sky views was bracketed by views of the calibration blackbodies, one at ambient temperature T_{amb} (typically −10 to −30 C) and one at T_{warm} = 10 C. Typically 30 blackbody or sky interferograms were co-added at each angle. Taking into account the calibration measurements, one full angular scan (0°–45° views) could be completed in approximately five minutes.

[10] Calibrated radiance spectra were obtained using the formula of *Revercomb et al.* [1988],

$$L_{sky}(\nu, \mu) = \mathrm{Re}\left\{ \left[\frac{I'_{sky}(\mu) - I'_{amb}}{I'_{warm} - I'_{amb}} \right] \right.$$
$$\left. \cdot \left[L_{warm}(\nu) - B(\nu, T_{amb}) \right] + B(\nu, T_{amb}) \right\}, \qquad (1)$$

where I' are complex valued Fourier transforms of unapodized interferograms recorded by the UPS-FTIR, L_{warm} is the radiance originating from the warm blackbody with nonunity emissivity (described below), and $B(\nu, T_{amb})$ is the Planck function evaluated at T_{amb}, the temperature of the ambient blackbody. These spectra contain errors associated with noise, precision, and accuracy, all of which we have tried to characterize.

[11] The critical factor for noise is the number of co-adds per spectrum, which at 30 resulted in a noise equivalent spectral radiance (NESR, the standard deviation of calibrated spectra of a uniform scene) of about 0.1 mW/(m^2 sr cm^{-1}). The most critical factors influencing precision and
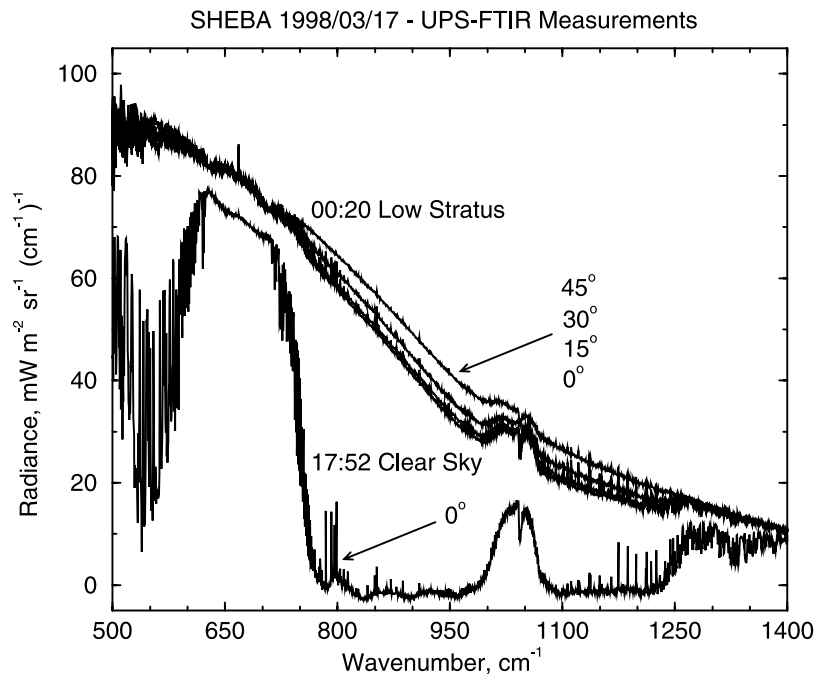
SHEBA 1998/03/17 - UPS-FTIR Measurements

Figure 1. Four upper curves: multiangle set of downwelling radiance spectra acquired by the UPS-FTIR on 17 March 1998 during the SHEBA campaign, under a low stratus cloud deck. Lower curve: zenith downwelling radiance spectrum collected later on the same day, under clear sky.

accuracy are the emissivity and temperature of the calibration blackbodies [*Walden et al.*, 1998].

[12] A frequency-dependent emissivity, $\varepsilon(\nu)$, of the warm blackbody was measured by taking spectra of it using the Polar-AERI (courtesy of Von Walden). The average emissivity in the spectral range of interest ($500-1400$ cm^{-1}) is about 0.95. Assuming any light not emitted from the warm blackbody is reflected from the surroundings at ambient temperature, the radiance emerging from it is expressed as

$$L_{\text{warm}}(\nu) = \varepsilon(\nu)B(\nu, T_{\text{warm}}) + [1 - \varepsilon(\nu)]B(\nu, T_{\text{amb}}). \quad (2)$$

In fact, for cloudy scenes, the emissivity correction of equation (2) was found to be very slight. The temperature of the warm blackbody is monitored by resistance thermal detectors with a nominal precision of 0.1 K, calibrated against high accuracy mercury thermometers before and checked after the field campaign. On days in which a low-lying cloud was very thick, it was possible to evaluate the precision by assuming the cloud itself emitted as a blackbody. Examination of such spectra indicates a calibration error on the order of 0.15 K in terms of brightness temperature, which corresponds to a radiance precision of 0.2 mW/(m^2 sr cm^{-1}) at 800 cm^{-1}.

[13] A total of 76 multiangle sets were recorded with the UPS-FTIR on 22 days from 8 March to 19 April 1998. One example of a multiangle set is displayed in Figure 1, where calibrated downwelling radiances are plotted against wavenumber for the four angular views. It is complemented by an example of a spectrum of clear sky radiances downwelling from zenith (lowest curve).

[14] For the above period, helpful complementary data are available from a variety of other instruments for atmospheric research deployed at the SHEBA site. The most important for the present study are the profiles of temperature and humidity obtained from radiosondes and the cloud macro- and microphysical properties obtained from the depolarization lidar and cloud radar operated by the NOAA/Environmental Technology Laboratory [*Shupe et al.*, 2001]. As was revealed by the latter instruments [*Intrieri et al.*, 2002], March and April 1998 were characterized by a monthly averaged fraction of cloud occurrence of 85% and 93% above the SHEBA station, and a monthly averaged lowest cloud base height of 1.4 and 1.3 km, with most low-cloud bases below 1 km AGL. The monthly averaged occurrence of liquid water in clouds was 68% and 69%, respectively. *Intrieri et al.* [2002] also found that single layer clouds were most prevalent at that time.

3. Data Analysis
3.1. Geometric Method

[15] The geometric method exploits the angular dependence of radiance emitted by an overcast sky in order to obtain a single cloud temperature T_{cld} and an effective cloud optical depth spectrum, $\delta_{\text{eff}}(\nu)$. The measured spectral radiance, $L_{\text{sky}}(\nu, \theta)$, is expressed using an integrated form of the IR radiative transfer equation for a low cloud, as a sum of background radiation attenuated by the cloud and radiation emitted by the cloud:

$$L_{\text{sky}}(\nu, \mu) = B(\nu, T_{\text{bkg}})e^{-\delta_{\text{eff}}(\nu)/\mu} + B(\nu, T_{\text{cld}})\left[1 - e^{-\delta_{\text{eff}}(\nu)/\mu}\right]. \quad (3)$$

Here, μ is $\cos(\theta)$, θ is the viewing angle from zenith, and T_{bkg} is the sky's background radiative temperature. The high degree of simplification associated with this representation
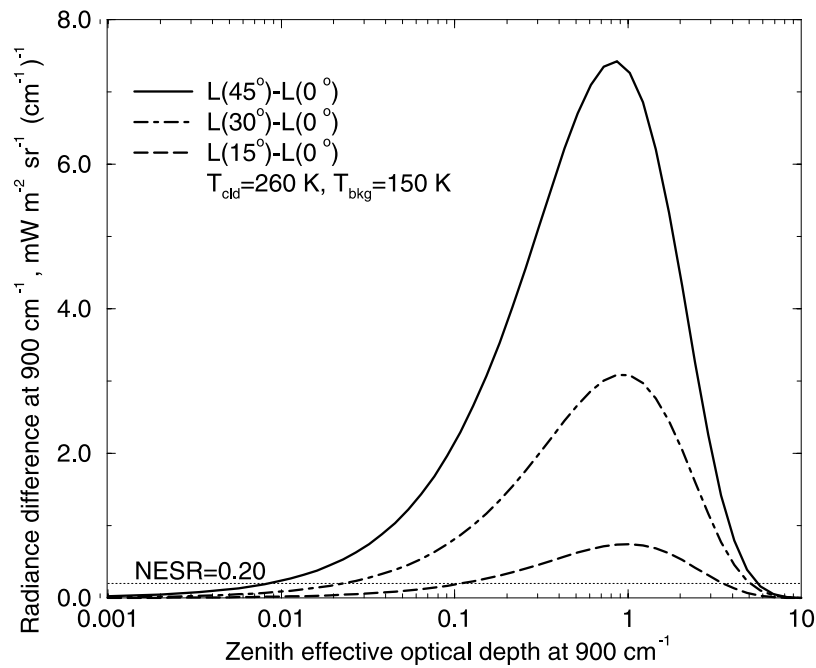
Figure 2. Difference at 900 cm^{-1} between radiances at two angles as a function of the effective cloud optical depth (δ_{eff}/μ) for T_{cld} = 260 K and T_{bkg} = 150 K, calculated with equation (3). The UPS-FTIR's NESR is indicated in the bottom.

is a result of several assumptions, the validity of which we now discuss.

3.1.1. Effect of Cloud Scattering

[16] The details of scattering are all contained in δ_{eff}, which in turn depends on optical properties of cloud particles, as well as on cloud temperature and reflection of radiation from the surface [e.g., *Rathke and Fischer*, 2002]. One assumption made in writing equation (3) is that δ_{eff} does not depend significantly on μ. We have studied this assumption by calculating the relative difference, $[\delta_{eff}(45°) - \delta_{eff}(0°)]/\delta_{eff}(0°)$, over a range of the parameters μ and Λ, where Λ is a function of the temperature difference between
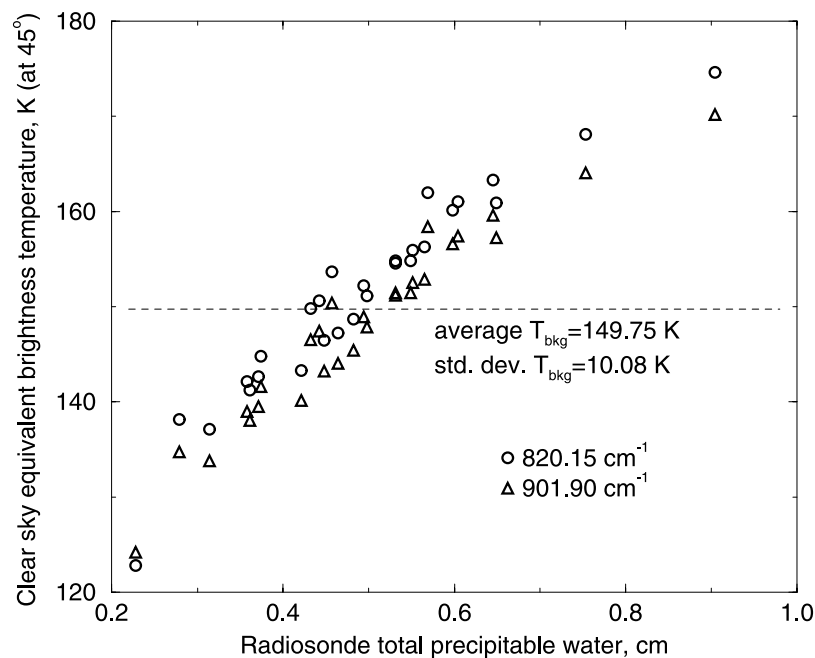
Figure 3. Clear sky equivalent brightness temperatures of the downwelling radiance reaching the surface at 45° in microwindows centered at 820 and 901 cm^{-1}, calculated from the SHEBA radiosonde temperature and moisture profiles for the days of the measurements.
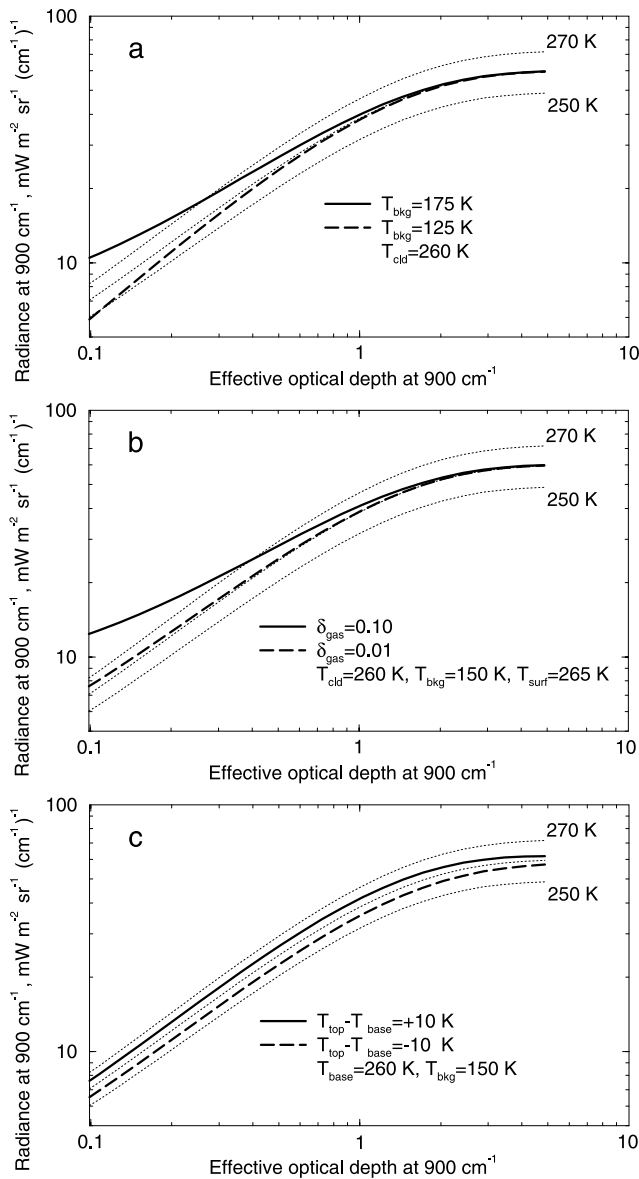
Figure 4. Influence of several effects and parameters on the relation between effective cloud optical depth (δ_{eff}/μ) and radiance $L(v,\mu)$ assumed for the geometrical method. The thin lines drawn in the background were obtained from equation (3) with different values of T_{cld} and with T_{bkg} = 150 K (this is the assumed curve form), for v = 900 cm^{-1}. (a) Influence of background radiation and the variation of its brightness temperature T_{bkg}. (b) Influence of gaseous absorption and emission between the cloud and the surface; δ_{gas} is the gas absorption optical depth. (c) Influence of a temperature gradient between cloud base and cloud top. The latter curves were calculated with equation (4).

cloud and surface, as described by *Rathke and Fischer* [2002]. Our calculations show that this relative difference is small enough (less than 1%) that we can ignore it for the present purpose.

3.1.2. Strength of the Signal in the Presence of Instrument Noise

[17] Figure 2 shows differences in radiance between various pairs of zenith angle views, calculated using equation (3), over several orders of magnitude of δ_{eff}. A benchmark comparison is the ratio of the 30°−0° radiance difference (the "signal"), as compared to one standard deviation in instrument noise (NESR, as defined above). This ratio is greater than two over optical depths in the range 0.05 to 4; Figure 2 also indicates that this range is extended if larger zenith angles are considered.

3.1.3. Significance and Form of the Background Radiance

[18] For a cloudless sky, the downwelling radiance within the 8–12 μm (770–1230 cm^{-1}) thermal window, outside of the 9.7 μm ozone band, is mainly attributable to broadband (continuum) emission from water vapor. In the radiative model (equation (3)), this contribution is represented as a "background" radiance, $B(v,T_{bkg})$. In the relatively cold and dry springtime Arctic atmospheres, this background term is usually very small, as can be seen by referring again to Figure 1. During the observation period, however, the total precipitable water (TPW) amount reached values of up to 0.9 cm, with an average of 0.5 cm; this gives rise to nonnegligible background radiances. Figure 3 shows values of clear-sky brightness temperatures calculated with the extended line-by-line atmospheric Transmittance and Radiance Algorithm (XTRA) radiative transfer model [*Rathke and Fischer*, 2000] for two microwindows. SHEBA radiosoundings were used as inputs to the model. The figure indicates an average brightness temperature for all days of approximately 150 K within the longer wavelength part of the thermal window (800–1000 cm^{-1}). This value decreases by less than 5 K for a view at 0° instead of 45°. Therefore the background radiance is represented in equation (3) with no angular dependence.

[19] Figure 4a shows another benchmark comparison, again as a function of δ_{eff}. Measurements at a given wavenumber will lie close together on lines like the thin dotted curves plotted in the background, which are for T_{bkg} = 150 K and T_{cld} = 250, 260, 270 K. The two thick lines show the effect when the extreme values found from Figure 3 are assigned to T_{bkg} instead of the average value 150 K. The significant dependence apparent in the figure for smaller δ_{eff} ● values, largely due to the transmitted background term, emphasizes the need to include this contribution in the model.

3.1.4. Radiative Effect of Gases Below the Cloud

[20] Since the radiative model ignores the effect of gases below the cloud, it is useful to examine the contribution of such gases to downwelling radiance in the Arctic during the observation period. Figure 5 shows the spectrum of δ_{gas}, the absorption optical depth of atmospheric gases in the lowest kilometer of the sub-Arctic winter standard atmosphere [*McClatchey et al.*, 1972], calculated by XTRA assuming a 45° viewing angle. The value of δ_{gas} is seen to be smaller than 0.01 in many microwindows within the 8–12 μm window. This value, implied by the 0.45 cm TPW in the sub-Arctic winter atmosphere, is consistent with the TPW values and cloud base-height estimates from the SHEBA radiosoundings for the observation period (see Figure 3). Figure 4b shows the effect on downwelling radiance due to two hypothetical intervening optical depths. Considering the curve for which δ_{gas} = 0.01, we conclude
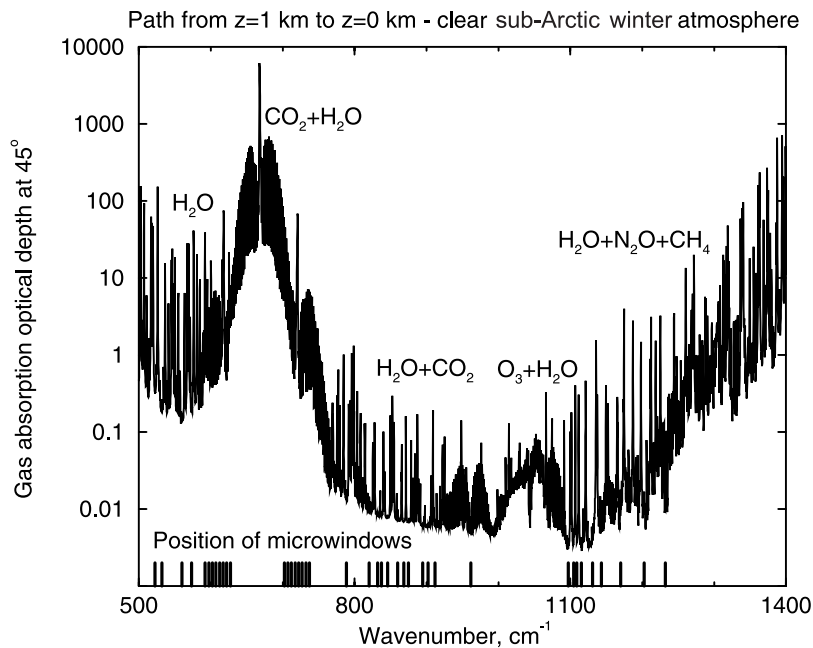
Figure 5. Calculated infrared spectra of the gas absorption optical depth through the lowest kilometer above the surface of the sub-Arctic winter atmosphere [*McClatchey et al.*, 1972], for a zenith viewing angle of 45°. The molecular species accounted for were H_2O, CO_2, O_3, N_2O and CH_4. The spectral resolution is $\Delta v = 0.25$ cm^{-1}. Vertical bars indicate the position of the microwindows used for the cloud parameter retrievals and of the CO_2 channels used for the cloud base height estimation.

that below-cloud gases can indeed be ignored in the Arctic springtime.

3.1.5. Effect of Vertical Temperature Structure

[21] SHEBA radiosoundings during the observation period frequently indicate in-cloud temperature gradients of $1-3$ K, with much larger gradients occasionally arising under strong inversions. The radiation model, equation (3), however, is that of an isothermal cloud with effective temperature T_{cld}. We therefore have repeated calculations with a modified version of equation (3) which includes emission by a vertically nonisothermal cloud,

$$
I(v,\mu) = B(v, T_{bkg})e^{-\delta_{eff}(v)/\mu}
$$
$$
+ \left\{ 1 - \frac{\mu}{\delta_{eff}(v)\ln\left[B(v,T_{top})/B(v,T_{base})\right]} \right\}^{-1} B(v, T_{base}).
$$
$$
\times \left[1 - e^{\ln\left[B(v,T_{top})/B(v,T_{base})\right]-\delta_{eff}(v)/\mu} \right]
$$

$$
(4)
$$

T_{base} and T_{top} are the cloud base and cloud top temperatures. The assumption inherent to this equation is an exponential-in-optical-depth dependence of the Planck function. Our results are displayed in Figure 4c. The thick lines shown in this figure were calculated with this equation for gradients of $+10$ K and -10 K. They indicate that for smaller values of δ_{eff}/μ, T_{cld} is approximately equal to the average of T_{base} and T_{top}, and that within the narrow range of δ_{eff}/μ produced by the measurements, T_{cld} can be regarded as constant.

3.1.6. Qualitative Discrimination of Plane-Parallel Clouds: The Straight-Line Criterion

[22] Our qualitative method of identifying plane-parallel clouds follows that of *Neshyba and Piedalue* [2000]. We

begin with an approximation of zero background radiance in equation (3), and rewrite it as

$$
\ln\left[1 - \frac{L(v,\mu)}{B(v,T_{cld})}\right] = -\delta_{eff}\frac{1}{\mu}. \qquad (5)
$$

A graph of the left hand side of equation (5) as a function of $1/\mu$ should produce a straight line with zero intercept and slope equal to $-\delta_{eff}$. Inspection of the result constitutes an initial, qualitative, "straight-line criterion" for discriminating homogeneous from inhomogeneous clouds. Since we do not know the correct cloud temperature a-priori to use in equation (5), we first evaluate B at the surface temperature. Although this approximation could be refined, we have found it unnecessary to do so: even a poor choice of T_{cld} still produces a straight line of the left hand side of equation (5) as a function of $1/\mu$, and therefore allows a clear discrimination between homogeneous and inhomogeneous cloudy scenes. The straight-line plots shown in Figure 6, for example, show one cloud scene that fails to meet the criterion, and another that meets the criterion.

3.1.7. Parameter Retrieval Algorithm

[23] Once a cloud scene is identified as being homogeneous according to the straight-line criterion, we suppose that no variables except μ vary within the course of an angular scan with the instrument. Thus we obtain at each frequency four measured radiances, which, with the help of equation (3), constitute a system of four nonlinear equations in unknowns δ_{eff}, T_{cld} and T_{bkg}. This approach is similar to *Taylor*'s [1974] method, in which the radiance is upwelling and T_{bkg} is the surface temperature. To reduce noise, radiance is first averaged over microwindows, i.e., spectral regions that fulfill the requirement $\delta_{gas} < 0.01$. As can be
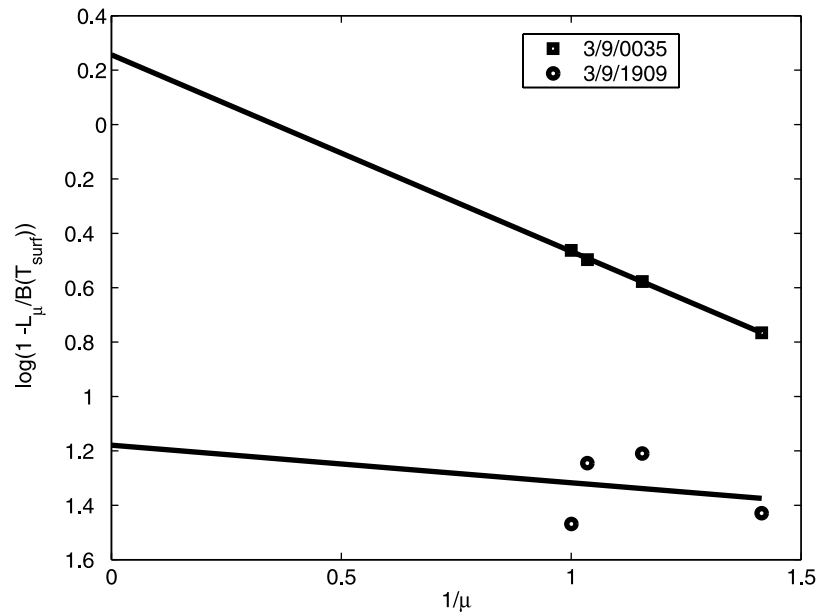
Figure 6. Left hand side of equation (5) as a function of $1/\mu$ for two cloudy multiangle datasets. Squares: 9 March 1998, at 00:35 UTC. Circles: 9 March 1998, at 19:09 UTC. Points lying on a straight line imply horizontally homogeneous cloud scene.

seen from Figure 5, at least 11 microwindows can be defined in this way, located between 820 and 963 cm^{-1}. A standard least squares solver is then used together with equation (3) to find, for each microwindow, values of the unknown parameters that minimize the sum of squared differences between the measured and calculated radiances for the four angles.

[24] It is evident that a cloud scene that is even slightly inhomogeneous will give rise to errors in retrieved values of cloud temperature and optical depth. For the purpose of a sensitivity analysis, the background temperature was set to zero, and the frequency was assumed to be 800 cm^{-1}. A set of four temperatures and optical depths were generated, randomly distributed about $\delta_{eff,0}$ values of 1, 2, and 3, with $T_{cld,0} = 300$ K. These distributions have standard deviations $\sigma_\delta = 0.05$ and $\sigma_T = 0.5$ K for optical depth and temperature, and together constitute simulated cloud distributions. They are indicated by pluses in Figure 7. Next, equation (3) was used to generate radiances for each of these pairs at angles of 0, 15, 30, and 45°. From these radiances, a single optical
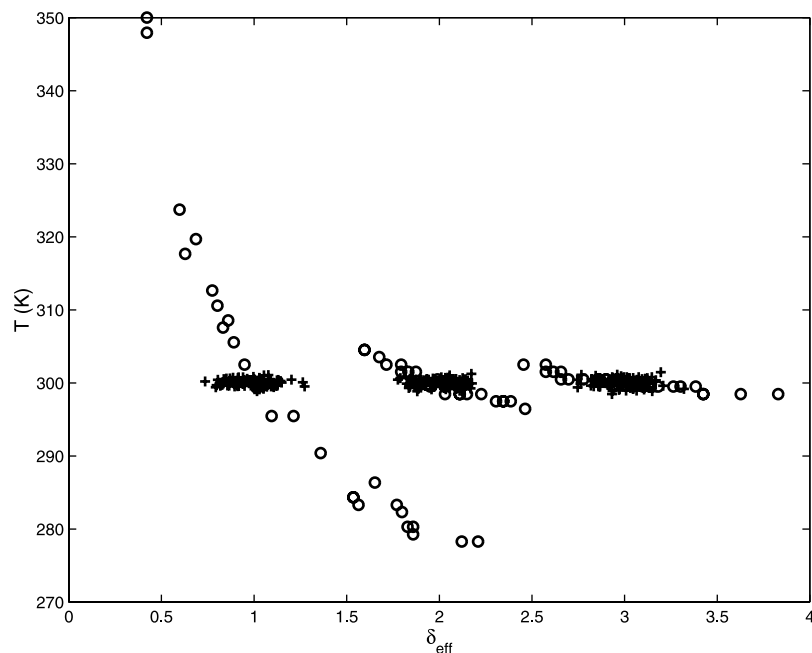

Figure 7. Retrieved cloud temperatures and effective optical depths (circles) based on 25 simulated inhomogeneous cloud scenes (pluses).

depth (δ_{eff}) and temperature (T_{cld}) were retrieved. Retrievals were done twenty-five times and led to the distribution of retrieved optical depths and temperatures, marked with circles in Figure 7.

[25] It is clear from Figure 7 that clouds with optical depths of 1 will produce a distribution of retrieved temperatures far in excess of actual values. Clouds with optical depths of 3, on the other hand, will produce a distribution of retrieved temperature comparable to the actual values. The information loss in the retrieval process can be described by the ratio $R(T) = \sigma_{T,\text{retrieved}}/\sigma_T$, and similarly for $R(\delta)$. For the cases considered, $R(T) = 20$, 4, and 1.5 for $\delta_{eff,0} = 1$, 2, and 3, respectively. The information loss corresponding to optical depth, $R(\delta)$, is about 4 in all three cases.

[26] The shape of these retrieved distributions can be related to the form of the effective emissivity equation when δ_{eff} is small enough that the exponential is well approximated by its first order expansion. In that case, the hyperbolic equation

$$L(\nu, \mu) \approx B(\nu, T_{cld})\delta_{eff}/\mu \qquad (6)$$

results. This bilinear form is clearly not suitable to recover unique values of $B(\nu, T_{cld})$ and δ_{eff}. Since $B(\nu, T_{cld})$ is a monotonic function of T_{cld}, the same comment applies to T_{cld}, i.e., retrieval of unique values of T_{cld} and δ_{eff} using multiangle data alone becomes ill posed as the optical depth becomes small.

[27] Other tests indicated that the retrieval of T_{bkg} is, because of $T_{bkg} \ll T_{cld}$, very sensitive to noise and also to slight horizontal inhomogeneities. Because of all these findings, T_{bkg} was fixed to 150 K (the average background temperature for the 11 microwindows, according to Figure 3) and the final retrieval algorithm was designed as a two-step approach. First, we did a two-parameter multiangle retrieval with the 820 cm^{-1} radiance data to find δ_{eff} and T_{cld} as described above. The 820 cm^{-1} microwindow was chosen because δ_{eff} values of liquid water and ice clouds are largest in this spectral region and hence T_{cld} most trustable there. We then used this T_{cld} as another fixed value in a second multiangle retrieval over all microwindows, retrieving only $\delta_{eff}(\nu)$.

3.1.8. Quantitative Discrimination and the Inhomogeneity Measure

[28] For the subset of clouds that pass the qualitative test for homogeneity, and for which we have obtained optimized parameters T_{cld} and δ_{eff}, we apply the following quantitative measures of cloud inhomogeneity:

$$\text{IM}_T = \left\{ \sum \Delta L^2 \bigg/ \sum \left(1 - e^{-\delta_{eff}/\mu}\right)^2 \right\}^{1/2} \frac{1}{dB(\nu, T_{cld})/dT_{cld}}, \qquad (7)$$

and

$$\text{IM}_\delta = \left\{ \sum \Delta L^2 \bigg/ \sum \left(\frac{e^{-\delta_{eff}/\mu}}{\mu}\right)^2 \right\}^{1/2} \frac{1}{B(\nu, T_{cld})}, \qquad (8)$$

where $\sum \Delta L^2$ is the sum of squared radiance errors (calculated-observed) for all viewing angles, using best-fit cloud parameters. The values of IM_T and IM_δ describe uncertainties in retrieved values of T_{cld} and δ_{eff}, respectively. Insofar as these values reflect actual variations in cloud properties (rather than instrumental noise), they may be interpreted as measures of the cloud's inhomogeneity.

3.2. Spectral Method

[29] The spectral method is based on a theoretical cloud model relating cloud microphysical properties to cloud spectral optical properties. These are input to a radiative transfer model, which calculates a radiance spectrum, accounting for all radiative transfer details, e.g., scattering, effects of thermal gradients, and absorption/emission of gases. An algorithm then tries to find the set of cloud microphysical properties for which the simulation best reproduces the measurements.

[30] The relevant cloud microphysical properties are: the cloud phase (liquid water and/or ice); the shape and orientation of the cloud particles; the particle size distribution, characterized by an effective particle radius r_{eff} (the ratio of the third to the second moment of the size distribution), and an effective variance v_{eff}; and the liquid and ice water contents, LWC and IWC. Vertically integrated, the latter yield the liquid and ice water paths, LWP and IWP. Optical properties needed by the radiative transfer model XTRA are: the extinction optical depth, δ, the single-scattering albedo, ω_0, and the asymmetry factor, g. The extinction optical depth of a liquid water cloud is, for example, related to LWP via $\delta_{liq} = \sigma_{ext,liq}\text{LWP}$, where $\sigma_{ext,liq}$ is the mass extinction coefficient.

[31] For clouds containing ice, there is the problem of defining an ice crystal habit sufficiently representative for all temperature ranges. *Korolev et al.* [1999], for example, recently found that 97% of the ice crystals in Arctic clouds exhibit a variety of nonpristine habits. This lack of knowledge about a representative habit has inclined us to represent here ice particles as a collection of "equivalent" spheres having the same surface-to-volume ratio, as suggested by *Grenfell and Warren* [1999]. This technique has the advantage that optical properties can be calculated from microphysical properties, as in the case of water droplets, with Mie theory. (Nevertheless, nonsphericity could change the results, especially for observations at larger viewing angles ($\theta > 70°$).) Lacking a-priori information about cloud vertical structure, we assumed the particle size distribution as well as LWC and IWC to be constant with height.

[32] Optical properties of liquid water and ice clouds ($\sigma_{ext,liq}$, $\sigma_{ext,ice}$, etc.) were specified with Mie theory from the tabulated refractive indices of liquid water [*Downing and Williams*, 1975] or ice [*Warren*, 1984] for clouds composed of spherical particles and distributed according to a *Hansen* [1971]-modified gamma size distribution. According to *Rathke and Fischer* [2000], σ_{ext}, ω_0 and g (and hence δ_{eff}) are relatively insensitive to the particular form and width of the size distribution; therefore we assigned a value of $v_{eff} = 0.10$ to the variance of the size distribution, as in the work of *Smith et al.* [1993].

[33] Our assumptions reduce the free microphysical parameters to $r_{eff,liq}$ and LWP in the case of liquid water
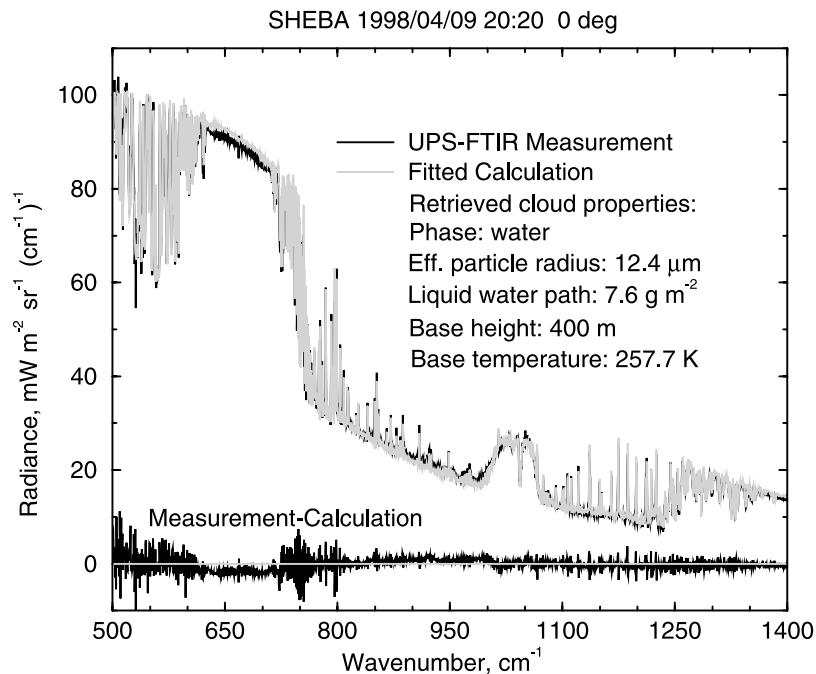
SHEBA 1998/04/09 20:20 0 deg

Figure 8. Observed and simulated spectra of downwelling radiance at 0° for 9 April 1998, at 20:20 UTC. The simulation is the product of the spectral method.

clouds, and to $r_{eff,ice}$ and IWP in the case of ice clouds. r_{eff} and LWP or IWP are retrieved from the radiance spectra by repeating forward simulations with the radiative transfer model XTRA for model atmospheres set up from radiosonde temperature and humidity profiles, and by inserting at some level with base temperature T_{base} a single cloud layer. The XTRA runs are used to improve iteratively r_{eff} and LWP values (as described by *Rathke and Fischer* [2000]), until the sum of squared differences between the measured and calculated equivalent brightness temperatures, the χ^2 cost function, is minimized.

[34] The application of the spectral method is not limited to "true" window channels (in contrast to the geometric method), with the advantage that channels located in the so-called "dirty" window around 560 cm^{-1} can also be included in the χ^2 function. This expanded spectral regime is useful for improved cloud phase discrimination [*Rathke et al.*, 2002]. Thus the *Rathke and Fischer* [2000] algorithm was extended to account also for radiances in several microwindows located in the 500–600 cm^{-1} region (the UPS-FTIR has a lower wavenumber cutoff at 500 cm^{-1}). For this purpose, XTRA was updated with the CKD_2.4 water vapor continuum model [*Tobin et al.*, 1999].

[35] The radiance in spectral regions where CO_2 is the dominant absorber is sensitive to cloud height [*Mahesh et al.*, 2001], and hence, accounting for "CO_2 channels" in the χ^2 function allows a retrieval of cloud base height (or temperature) consistent with the atmospheric vertical temperature structure reported by the radiosonde. The 700–740 cm^{-1} spectral range (according to the suggestion of *Mahesh et al.* [2001]) and, additionally, the 590–630 cm^{-1} spectral range (based on the same grounds) were included for cloud height determination.

[36] In practice, the retrieval with the spectral method was repeated twice, once for an all-liquid cloud and once for an all-ice cloud. Depending on the resulting χ^2 value, a cloud phase index ("liquid" or "ice") was attributed to the observations. The final products of the spectral method applied to a single radiance spectrum are: r_{eff}, and LWP or IWP, T_{cld}, cloud phase, and δ_{eff} (according to the definition of *Rathke and Fischer* [2002]).

4. Results

[37] Of the 76 multiangle datasets recorded by the UPS-FTIR in March and April 1998 at the SHEBA site, 18 were rejected as too inhomogeneous for the geometric analysis according to the straight-line criterion introduced in section 3.1.6, and further 23 sets were rejected after the parameter retrieval of section 3.1.7 because T_{cld} fell outside of a plausible range (230 K $< T_{cld} <$ 270 K). In the following, the remaining 35 datasets are referred to as the "homogeneous subset". Only for this subset will the results of the geometric method be presented.

[38] In contrast, the spectral method could be applied to all 76 multiangle sets. Figure 8 is presented to show the adequacy of the retrieved δ_{eff}-spectrum in reproducing the observed radiance. The mean standard deviation across the whole 8–12 μm window is 0.7 mW/(m^2 sr cm^{-1}), which is only slightly larger than the accuracy of the UPS-FTIR estimated in section 2. In the 20 μm window, the modeled spectrum also appears to match the recorded radiance well on average, though with a higher noise level. The spectral method identified this spectrum as pertaining to a predominantly liquid water cloud, with a base height of 400 ± 100 m and LWP = 7.6 g m^{-2}. For comparison, the multi-instrument technique of *Shupe et al.* [2001] identified
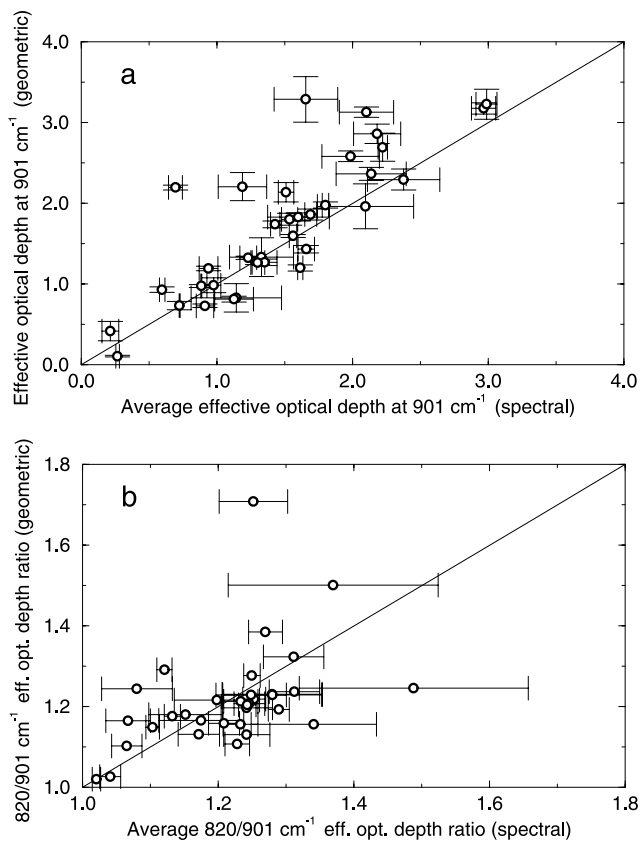
Figure 9. (a) Effective cloud optical depths at 901 cm^{-1} obtained from the geometric method versus the spectral method. (b) Ratio of the effective cloud optical depths at 820 cm^{-1} and 901 cm^{-1} obtained from the geometric method versus the spectral method.

this as a liquid-phase cloud with ice precipitation, and with $z_{base} = 268-328$ m and LWP = $5.0-12.9$ g m^{-2}.

4.1. Comparison of $\delta_{eff}(\nu)$ Determined With Geometric and Spectral Methods

[39] In Figure 9a, we have compared $\delta_{eff}(901$ cm$^{-1})$ derived with the geometric method and $[\delta_{eff}(901$ cm$^{-1},0°)$ $+ \delta_{eff}(901$ cm$^{-1},45°)]/2$ determined with the spectral method for the entire homogeneous subset. The width of the bars along the **x** axis corresponds to $|\delta_{eff}(901$ cm$^{-1},0°)$ $- \delta_{eff}(901$ cm$^{-1},45°)|$, and along the y axis it corresponds to $2IM_\delta$. In Figure 9b we also present the comparison of the ratio $\delta_{eff}(820$ cm$^{-1})/\delta_{eff}(901$ cm$^{-1})$ determined with both methods, which is a function of cloud phase and particle size [*Rathke and Fischer*, 2002]. The width of the bars along the **x** axis corresponds in this case to $|\delta_{eff}(820$ cm$^{-1},0°)/\delta_{eff}(901$ cm$^{-1},0°) - \delta_{eff}(820$ cm$^{-1},45°)/\delta_{eff}(901$ cm$^{-1},45°)|$. Root-mean-square deviations between the results of the geometric and spectral methods are 52% and 24%, respectively. These rms deviations reduce to 15% and 7% for the 16 cases in which the deviation of the retrieved cloud temperatures was less than 2.5 K. The agreement is better for the effective cloud optical depth ratio, because absolute errors at both wavenumbers sometimes cancel. The range of infrared optical depths found here is similar to that

reported by *Pinto et al.* [1997], also for springtime Arctic clouds.

4.2. Comparison With Cloud Temperatures Inferred From Lidar/Radiosonde Data

[40] We have also compared T_{cld} derived with the geometric method and $T_{cld}(0°)$ determined with the spectral method with cloud temperatures obtained from lidar/radiosonde data (Figure 10). The latter were determined by interpolating the lidar cloud base heights to radiosonde profiles nearest in time. In cases where the cloud base height was too low to be resolved by the lidar, a "radiosonde only" cloud temperature was estimated as the temperature at a height of 0.1 km.

[41] In Figure 10a, the width of the error bars in the vertical direction corresponds to $2IM_T$. The corresponding standard deviations are 5.1 K and 2.9 K for the homogeneous subset. This indicates that the spectral method matches the lidar/radiosonde record better than does the geometric method. Some deviations can be explained by the fact that both methods retrieve an effective cloud radiative temperature, which differs from the cloud base temperature in the presence of strong in-cloud temperature gradients (as discussed in section 3.1.5). The retrieval with the spectral method sometimes failed for clouds based above 2 km because of inadequate vertical resolution. Interestingly, deviations are not correlated with the occurrence of ice
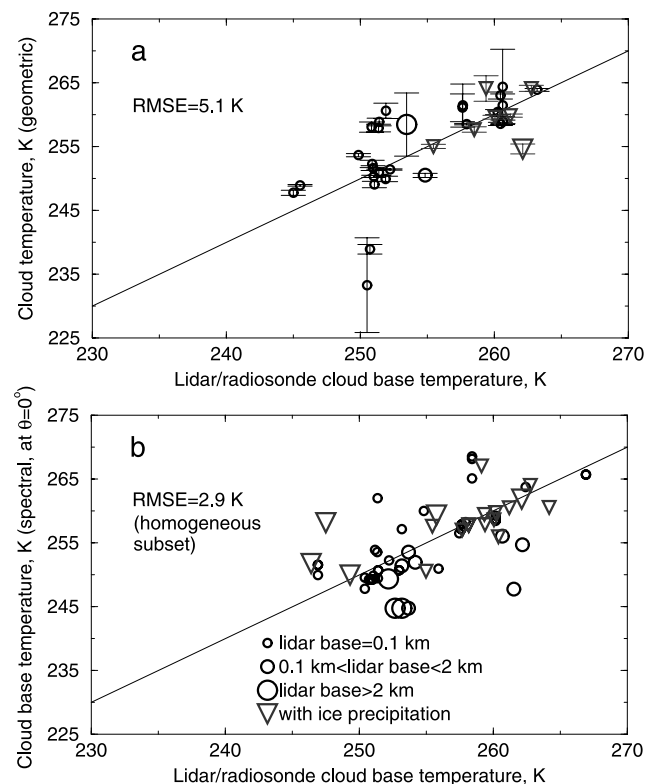

Figure 10. (a) Comparison of effective cloud temperatures obtained from the geometric method versus lidar/radiosonde values. (b) Comparison of cloud base temperatures obtained from the spectral method versus lidar/radiosonde values.
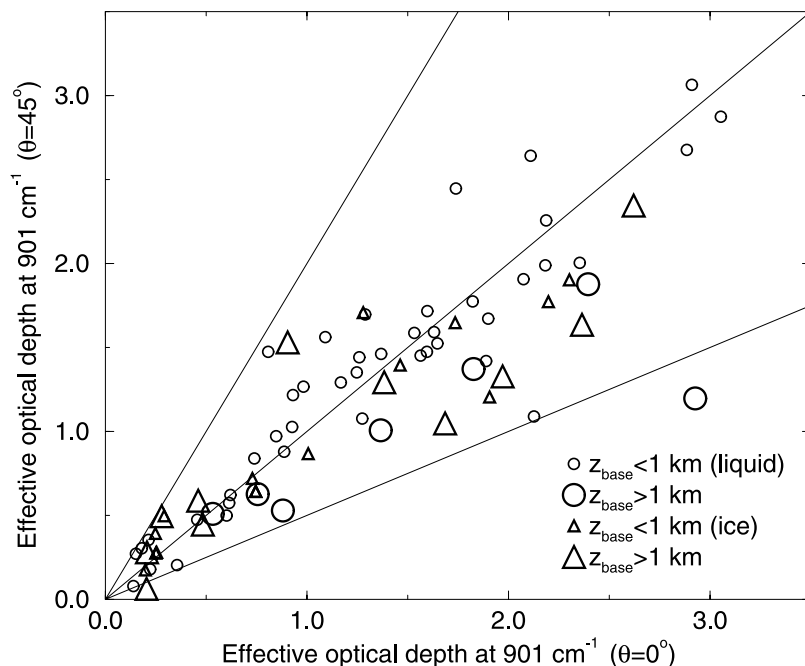
Figure 11. Comparison of effective optical depths at $\theta = 0°$ versus $45°$ (spectral method).

precipitation, indicating that this precipitation generally had negligible infrared absorption.

4.3. Sources of Cloud Horizontal Inhomogeneity

[42] Figures 11 and 12 explore the origin of cloud inhomogeneity using results from the spectral method alone, by plotting parameters retrieved at $\theta = 0°$ versus $45°$, with different symbols to indicate cloud height and phase. The changes in optical depth from $\theta = 0°$ to $45°$ can be substantial (Figure 11) but are not correlated with z_{base}. In relative terms, the variability in optical depth appearing in Figure 11 shows up in the retrieved particle effective radius (Figure 12a) and condensed water path (Figure 12b). In contrast, the cloud temperature (Figure 12c) exhibits much less relative variability. The average spherical particle effective radius is 10.8 μm for clouds identified as predominantly liquid (50 samples) and 17.6 μm for clouds identified as predominantly ice (26 samples). The standard deviation in the effective radius is smaller than the standard deviation in IWP or LWP, which indicates that the cloud's radiative inhomogeneity is primarily caused by the horizontal variability in cloud water content. These observations are consistent with most measurements [*Fu et al.*, 2000; *Benner et al.*, 2001].

4.4. Estimation of Downwelling Longwave Fluxes

[43] With the availability of the multiangle datasets, the influence of cloud horizontal inhomogeneity on downwelling longwave fluxes can be estimated for the spectral range of the UPS-FTIR. The approach we used is similar to the one of *Lubin et al.* [1995]. First, downwelling radiance spectra $L(v,\mu)$ and a flux spectrum $F(v)$ were calculated with XTRA for a cloud with the mean parameters of the SHEBA dataset (phase = liquid, r_{eff} = 10.8 μm, LWP = 20 g m^{-2}, z_{base} = 1 km) inserted in the sub-Arctic winter standard atmosphere. Second, spectral radiance-to-flux conversion

factors $C(v,\mu)$ at the spectral resolution of the UPS-FTIR were determined from

$$C(v,\mu) = \frac{F(v)}{L(v,\mu)}. \tag{9}$$

And third, measured fluxes were computed once from observations at a single angle

$$F_i(v) = C(v,\mu_i)L_{sky}(v,\mu_i) \tag{10}$$

(assuming cloud horizontal homogeneity, these constitute "plane-parallel" flux estimates), and once from observations at all angles

$$\langle F(v)\rangle = \frac{1}{4}\sum_{i=1}^{4} C(v,\mu_i)L_{sky}(v,\mu_i). \tag{11}$$

$\langle F\rangle$ accounts for cloud horizontal inhomogeneity at the four considered angles along the actual azimuthal direction. (Note that the $C(v,\mu)$ are most accurate for clouds with the above parameters; nevertheless, they allow an estimation of the downwelling fluxes for clouds with other parameters, which is our present purpose.)

[44] The spectrally integrated values of F_i and $\langle F\rangle$ determined from the 76 datasets with equations (10) and (11) are compared in Figure 13. We infer from this figure that estimating downwelling longwave fluxes from radiance measurements at a single angle can lead to noticeable errors in the estimated fluxes. For the homogeneous subset, the average absolute difference between F_i and $\langle F\rangle$ is 2.4 W m^{-2} (which is close to the 1.8 W m^{-2} calculated by *Benner et al.* [2001]), while for the other cases it is 4 W m^{-2}. In some cases the difference can be as large as 13.7 Wm^{-2}, or
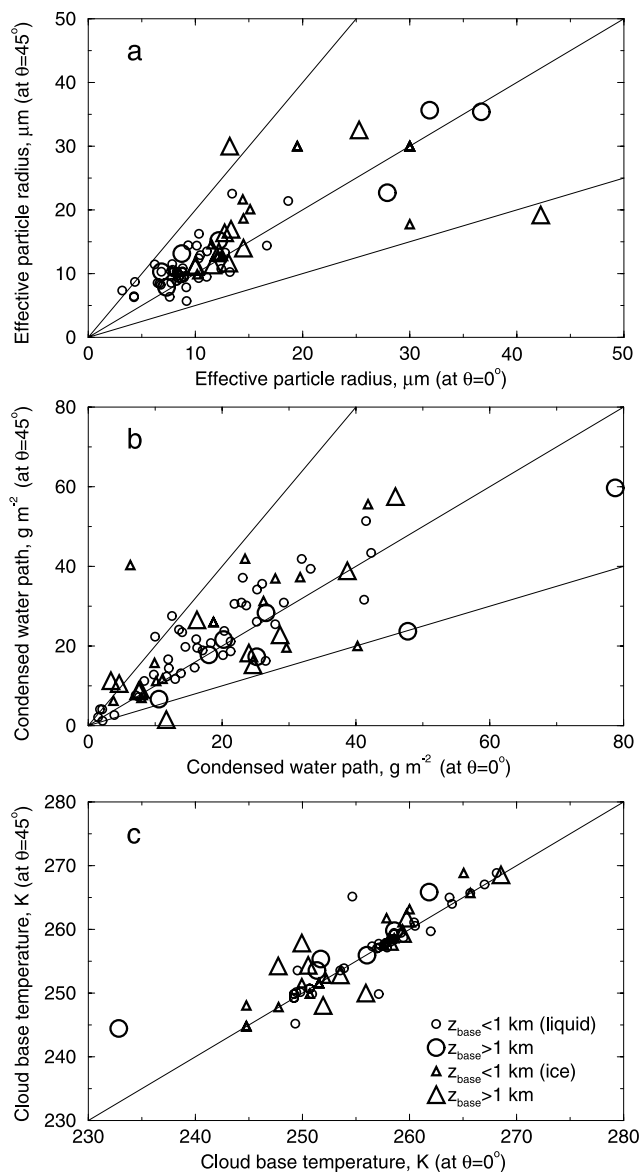
Figure 12. Comparison of (a) retrieved particle radius, (b) condensed water path, and (c) cloud base temperature at $\theta = 0°$ versus $45°$ (spectral method).

6.5% of the total downwelling longwave flux, and amounts to 24% of the flux integrated across the atmospheric windows between $500-600$ cm^{-1} and $750-1250$ cm^{-1}. Because no cloud signal contributes from outside the spectral range of the UPS-FTIR, this difference constitutes a) the effect of horizontal IR cloud optical depth changes on the instantaneous longwave cloud radiative forcing at the surface, and b) the potential error in the instantaneous longwave cloud forcing that could result if radiance measurements at a single angle were used to infer fluxes. Moreover, considering that the spectra were obtained under overcast skies and homogeneous cloud temperature conditions, this difference can be attributed unambiguously to horizontal variations in cloud microphysical properties (essentially liquid or ice water content). Our multiangle experiment has thus revealed that cloud water content variability can also be a matter of concern for the inter-

pretation of longwave radiation measurements of stratus clouds.

5. Conclusions

[45] In order to derive properties of Arctic stratus clouds from multiangle downwelling infrared radiance observations made by the UPS-FTIR at the SHEBA ice camp in March–April 1998, the geometric method was introduced and compared to the more established spectral method. The results showed that under conditions in which the plane-parallel assumption appears well founded, the geometric method can determine the effective temperature of the cloud, as well as an accurate effective optical depth spectrum. The geometric method is attractive because its application is particularly straightforward and independent of auxiliary data, and because the number of assumptions that need to be made about the condensate is small. With this, the geometric method is clearly of interest for automated retrievals of cloud properties from stand-alone surface based infrared sensors, and for remote sensing of Arctic mixed-phase clouds, which usually requires modifications to existing single-phase retrieval schemes [*Pinto et al.*, 1997; *Shupe et al.*, 2001].

[46] The spectral method offers other advantages. For example, it is the only method with which we can exploit radiance observations in the 20 μm dirty window, because it accounts for below-cloud atmospheric water vapor absorption. With its help, all the 76 multiangle datasets could be analyzed and an average effective radius of 10.8 μm determined for clouds identified as predominantly liquid. It is worth mentioning that this value agrees with findings of *Lubin and Simpson* [1997] for summertime Arctic stratus clouds, and with different results reported by *Shupe et al.* [2001].

[47] Our investigations of the sources for the limitations of the geometric method have revealed that Arctic stratus clouds may not be very homogeneous in the horizontal in
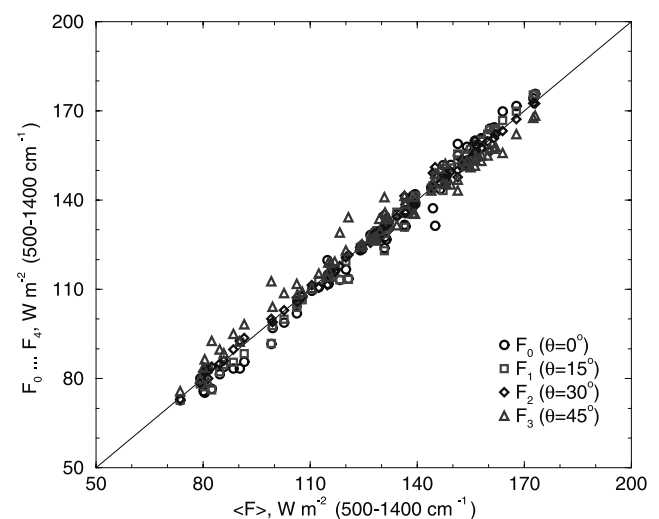

Figure 13. Comparison of average downwelling fluxes (integrated over the interesting $500-1400$ cm^{-1} spectral range of the UPS-FTIR) computed from radiance measurements at $\theta = 0, 15, 30,$ and $45°$ versus individual fluxes computed from measurements at one angle.

terms of infrared optical depth. Another conclusion of this study is therefore that the multiple-angle measurements presented here are a step towards making quantitative statements about the adequacy of the plane-parallel assumption for calculating longwave fluxes. The accuracy of the plane-parallel assumption over a horizontal range of $0.1-5$ km could be tested with the multiangle datasets: in about one half of the measurements, the horizontal inhomogeneity in one azimuthal direction was important and responsible for flux changes of typically 4 W m^{-2}. We expect this value to be a conservative estimate of the potential effect of the microphysical inhomogeneity of stratus clouds on downwelling longwave fluxes, because of our choice of cases appearing plane-parallel. *Lubin and Simpson* [1997] have estimated this same effect it to be of the order of $20-30$ W m^{-2} for Arctic summertime conditions. Considering that cloud temperatures are higher in the summertime, their observations are consistent with the 13.7 W m^{-2} found by us in specific cases.

[48] Improvements over the present multiangle infrared measurements could essentially be achieved by increasing the angular resolution in the zenith direction and by sampling different azimuth directions (for example, by using an imaging infrared radiometer or spectrometer). Having more samples would weaken some of the restrictions of the geometric method. And it would allow to study more precisely the horizontal variability of the infrared radiative properties of clouds and its impact on the downwelling longwave flux, which dominates the surface radiation balance in the polar regions during much of the year. Quantifying more precisely this effect is the purpose of ongoing work.

References

Benner, T. C., J. A. Curry, and J. O. Pinto, Radiative transfer in the summertime Arctic, *J. Geophys. Res.*, *106*, 15,173–15,183, 2001.

Curry, J. A., W. B. Rossow, D. Randall, and J. L. Schramm, Overview of Arctic cloud and radiation characteristics, *J. Clim.*, *9*, 1731–1764, 1996.

Diner, D. J., G. P. Asner, R. Davies, Y. Knyazikhin, J.-P. Muller, A. W. Nolin, B. Pinty, C. B. Schaaf, and J. Stroeve, New directions in earth observing: Scientific applications of multiangle remote sensing, *Bull. Am. Meteorol. Soc.*, *80*, 2209–2228, 1999.

Downing, H. D., and D. Williams, Optical constants of water in the infrared, *J. Geophys. Res.*, *80*, 1656–1661, 1975.

Francis, J., A method to derive downwelling longwave fluxes at the Arctic surface from TIROS operational vertical sounder data, *J. Geophys. Res.*, *102*, 1795–1806, 1997.

Fu, Q., B. Carlin, and G. Mace, Cirrus horizontal inhomogeneity and OLR bias, *Geophys. Res. Lett.*, *27*, 3341–3344, 2000.

Grenfell, T. C., and S. G. Warren, Representation of a nonspherical ice particle by a collection of independent spheres for scattering and absorption of radiation, *J. Geophys. Res.*, *104*, 31,697–31,709, 1999.

Hansen, J. E., Multiple scattering of polarized light in a planetary atmosphere, II, Sunlight reflected by terrestrial water clouds, *J. Atmos. Sci.*, *28*, 1400–1426, 1971.

Intrieri, J. M., M. D. Shupe, T. Uttal, and B. J. McCarty, Annual cycle of Arctic cloud geometry and phase from radar and lidar at SHEBA, *J. Geophys. Res.*, *107*(C10), 8029, doi10.1029/2000JC000423, 2002.

Korolev, A. V., G. A. Isaac, and J. Hallett, Ice particle habits in Arctic clouds, *Geophys. Res. Lett.*, *26*, 1299–1302, 1999.

Lubin, D., and A. S. Simpson, Measurement of surface radiation fluxes and cloud optical properties during the 1994 Arctic Ocean Section, *J. Geophys. Res.*, *102*, 4275–4286, 1997.

Lubin, D., D. Cutchin, W. Conant, H. Grassl, U. Schmid, and W. Biselli, Spectral longwave emission in the tropics: FTIR measurement at the sea surface and comparison with fast radiation codes, *J. Clim.*, *8*, 286–295, 1995.

Mahesh, A., V. P. Walden, and S. G. Warren, Ground-based infrared remote sensing of cloud properties over the Antarctic plateau, I, Cloud base heights, *J. Appl. Meteorol.*, *40*, 1265–1278, 2001.

Makshtas, A. P., and R. Korsnes, Distribution of solar radiation in the Barents Sea marginal ice zone during summer, *J. Geophys. Res.*, *106*, 2531–2543, 2001.

McClatchey, R. A., R. W. Fenn, J. E. A. Selby, F. E. Volz, and J. S. Goring, Optical properties of the atmosphere, *Environ. Res. Pap. 411*, 108 pp., Air Force Geophys. Lab., Hanscom AFB, Mass., 1972.

Neshyba, S., and A. Piedalue, Comparison of spectral and geometric methods for retrieving cloud parameters from downwelling FTIR spectra in the Arctic, paper presented at 6th Biennial HITRAN Conference, Harvard-Smithsonian Cent. for Astrophys., Cambridge, Mass., 2000.

Pinto, J. O., J. A. Curry, and C. W. Fairall, Radiative characteristics of the Arctic atmosphere during spring as inferred from ground-based measurements, *J. Geophys. Res.*, *102*, 6941–6952, 1997.

Prata, A. J., and I. J. Barton, A multichannel, multiangle method for the determination of infrared optical depth of semitransparent high cloud from an orbiting satellite, I, Formulation and simulation, *J. Appl. Meteorol.*, *32*, 1623–1637, 1993.

Rathke, C., and J. Fischer, Retrieval of cloud microphysical properties from thermal infrared observations by a fast iterative radiance fitting method, *J. Atmos. Oceanic Technol.*, *17*, 1509–1524, 2000.

Rathke, C., and J. Fischer, Efficient parameterization of the infrared effective beam emissivity of semitransparent atmospheric layers, *J. Geophys. Res.*, *107*(D4), 4035, doi:10.1029/2001JD000596, 2002.

Rathke, C., W. Armbruster, J. Fischer, E. Becker, and J. Notholt, Comparison of stratus clouds derived from coincident airborne visible and ground-based infrared spectrometer measurements, *Geophys. Res. Lett.*, *27*, 2641–2644, 2000.

Rathke, C., J. Fischer, S. Neshyba, and M. Shupe, Improving IR cloud phase determination with 20 microns spectral observations, *Geophys. Res. Lett.*, *29*(8), 1209, doi:10.1029/2001GL014594, 2002.

Revercomb, H. E., H. Buijs, H. B. Howell, D. D. Laporte, W. L. Smith, and L. A. Sromovsky, Radiometric calibration of IR Fourier transform spectrometers: Solution to a problem with the High Spectral Resolution Interferometer Sounder, *Appl. Opt.*, *27*, 3210–3218, 1988.

Shupe, M. D., T. Uttal, S. Y. Matrosov, and A. S. Frisch, Cloud water contents and hydrometeor sizes during the FIRE-Arctic Clouds Experiment, *J. Geophys. Res.*, *106*, 15,015–15,028, 2001.

Smith, W. L., X. L. Ma, S. A. Ackerman, H. E. Revercomb, and R. O. Knuteson, Remote sensing cloud properties from high spectral resolution infrared observations, *J. Atmos. Sci.*, *50*, 1708–1720, 1993.

Taylor, F. W., Remote temperature sounding in the presence of cloud by zenith scanning, *Appl. Opt.*, *13*, 1559–1566, 1974.

Thorndike, A., A toy model linking atmospheric thermal radiation and sea ice growth, *J. Geophys. Res.*, *97*, 9401–9410, 1992.

Tobin, D. C., et al., Downwelling spectral radiance at the SHEBA ice station: Water vapor continuum measurements from 17 to 26 μm, *J. Geophys. Res.*, *104*, 2081–2092, 1999.

Uttal, T., et al., Heat Budget of the Arctic Ocean, *Bull. Am. Meteorol. Soc.*, *83*, 255–275, 2002.

Walden, V. P., S. G. Warren, and F. J. Murcray, Measurements of the downward longwave radiation spectrum over the Antarctic Plateau and comparisons with a line-by-line radiative transfer model for clear skies, *J. Geophys. Res.*, *103*, 3825–3846, 1998.

Warren, S. G., Optical constants of ice from the ultraviolet to the microwave, *Appl. Opt.*, *23*, 1206–1225, 1984.

———————————

S. Neshyba, Chemistry Department, University of Puget Sound, 1500 N. Warner, Tacoma, WA 98416-1030, USA. (nesh@ups.edu)

C. Rathke, Institut für Weltraumwissenschaften, Freie Universität Berlin, Carl-Heinrich-Becker-Weg 6-10, D-12165 Berlin, Germany. (rathkec@zedat.fu-berlin.de)

A. Rivers, Cooperative Institute for Research in Environmental Sciences, University of Colorado, Campus Box 216, Boulder, CO 80309-0216, USA. (raaron@cires.colorado.edu)

P. Rowe, Department of Chemistry, Box 351700, University of Washington, Seattle, WA 98195-1700, USA. (prowe@u.washington.edu)

M. Shupe, Science and Technology Corporation, NOAA/Environmental Technology Laboratory, 325 Broadway, Boulder, CO 80305, USA. (Matthew.Shupe@noaa.gov)